Lesion-informed connectome diffusion modelling for individualized prediction of post-stroke brain atrophy

Gaolang Gong

gaolang.gong@bnu.edu.cn

Beijing Normal University https://orcid.org/0000-0001-5788-022X

Jing Yang

Beijing Normal University

Yixin Gao

Beijing Normal University

Liyuan Yang

Tianjin Normal University

Yaya Jiang

Beijing International Studies University

Wan Bin

University Hospitals of Genève

Şeyma Bayrak

Max Planck Institute for Human Cognitive and Brain Sciences

Xinyu Liang

Fudan University

Sofie Valk

Max Planck Institute for Human Cognitive and Brain Sciences

Maurizio Corbetta

Padova Neuroscience Center (PNC), University of Padova

Article

Keywords: Stroke, Individualized prediction, Brain atrophy, Structural connectome, Network diffusion modelling, Computational neuroimaging

Posted Date: August 5th, 2026

DOI: https://doi.org/10.21203/rs.3.rs-9954362/v1

Additional Declarations: There is **NO** Competing Interest.

Lesion-informed connectome diffusion modelling for individualized prediction of post-stroke brain atrophy

Jing Yang[1,†], Yixin Gao[1,†], Liyuan Yang[4], Yaya Jiang[5], Bin Wan[6,7], Şeyma Bayrak[7,8], Xinyu Liang[9], Sofie L. Valk[7,10,11], Maurizio Corbetta[12,13], Gaolang Gong[1,2,3]

[†]These authors contributed equally to this work.

Abstract

Remote brain atrophy after stroke is clinically consequential but difficult to predict at the individual-patient level. Here we developed a lesion-informed connectome diffusion modelling framework to forecast distributed grey matter volume (GMV) atrophy after focal stroke. Using longitudinal MRI data from two stroke cohorts spanning the hyperacute, subacute and chronic stages, we first showed that post-stroke GMV atrophy was more strongly constrained by structural than by functional connectivity. We then initialized network diffusion models with each patient's lesion map and found that the resulting simulations captured individualized atrophy patterns at 3 and 12 months post-stroke, whereas model performance was weak within the first week after stroke. The model-derived propagation stage was not a simple proxy for chronological time, but varied with lesion topography, lesion size, structural-network topology and the molecular context of lesioned regions. Finally, lesion-derived features enabled out-of-sample prediction of individualized atrophy patterns without requiring longitudinal imaging. These findings establish a computational framework for forecasting remote structural degeneration after stroke from early lesion information, with potential utility for patient stratification and individualized monitoring.

Author affiliations:

1 State Key Laboratory of Cognitive Neuroscience and Learning & IDG/McGovern Institute for Brain Research, Beijing Normal University, Beijing 100875, China

2 Beijing Key Laboratory of Brain Imaging and Connectomics, Beijing Normal University, Beijing 100875, China

3 Chinese Institute for Brain Research, Beijing 102206, China

4 Faculty of Psychology, Tianjin Normal University, Tianjin 300387, China

5 School of Artificial Intelligence and Language Sciences, Beijing International Studies University, Beijing 100024, China

6 Department of Psychiatry, University Hospitals of Genève, 1226 Thonex, Switzerland

7 Max Planck Institute for Human Cognitive and Brain Sciences, 04103 Leipzig, Germany

8 Department of Radiation Oncology, University Medical Centre Leipzig, 04103 Leipzig, Germany

9 Institute of Science and Technology for Brain-inspired Intelligence, Fudan University, Shanghai 200433, China

10 Institute of Neuroscience and Medicine (INM-7: Brain and Behaviour), Research Centre Jülich, 52428 Jülich, Germany

11 Institute of Systems Neuroscience, Heinrich Heine University Düsseldorf, 40225 Düsseldorf, Germany

12 Padova Neuroscience Centre, University of Padova, 35129 Padova, Italy

13 Neurology Department, UMC Utrecht Brain Centre, University Medical Centre Utrecht, Utrecht 3584 CX, the Netherlands

Correspondence to: Gaolang Gong

Address: National Key Laboratory of Cognitive Neuroscience and Learning IDG/McGovern Institute for Brain Research, Beijing Normal University, Beijing 100875, China

E-mail: gaolang.gong@bnu.edu.cn

Running title: Connectome-based prediction of post-stroke atrophy

Keywords: Stroke; Individualized prediction; Brain atrophy; Structural connectome; Network diffusion modelling; Computational neuroimaging

Introduction

Remote brain atrophy after stroke is clinically consequential but remains difficult to forecast at the individual-patient level. Although stroke starts as a focal vascular event, its structural consequences often extend to regions far from the primary lesion[1–3]. Neuroimaging studies have shown that grey matter loss, cortical thinning and white matter abnormalities can emerge in remote areas, indicating that post-stroke degeneration is not confined to locally injured tissue. These changes have been linked to motor recovery, cognitive performance and overall functional outcome[4–8], yet current imaging approaches provide limited ability to translate early lesion information into individualized predictions of later whole-brain structural degeneration. A central biomedical challenge is therefore to develop interpretable models that forecast how a focal lesion may give rise to distributed brain atrophy over time.

Post-stroke atrophy is likely multifactorial, involving local ischaemic and vascular factors as well as inflammatory and metabolic cascades[9–11]. Beyond these local influences, focal injury may induce downstream abnormalities in regions anatomically connected to the lesion site[12–15]. Consistent with this view, remote post-stroke atrophy has been observed in regions connected to the primary lesion, in keeping with diaschisis and transneuronal degeneration[14,16–20]. However, direct lesion-to-region links alone do not fully account for the broader and more distributed atrophy observed across the brain. Individualized forecasting therefore requires models that treat the lesion not only as a local anatomical defect, but as an initial perturbation embedded within a large-scale structural network.

Mechanistic network models provide a way to convert lesion location into whole-brain predictions of downstream structural change. Coordinated deformation modelling (CDM)[21] tests whether regional atrophy patterns are constrained by connectivity among brain regions, whereas network diffusion modelling (NDM) simulates how a focal perturbation may propagate through the graph structure of the connectome[22,23]. In neurodegenerative and psychiatric disorders, such models have shown that grey matter abnormalities often follow network-constrained patterns, in some cases with specific regions identified as putative epicentres[24–26]. However, most applications have relied on cross-sectional, group-level analyses, leaving unresolved whether these models can support patient-specific prediction of longitudinal atrophy after a focal brain lesion.

Longitudinal stroke imaging provides a stringent setting in which to evaluate such a framework. Lesion location, size and laterality vary substantially across patients, creating heterogeneous

patient-specific starting points for secondary degeneration[16,27,28]. If structural networks impose a generalizable rule on post-stroke atrophy, this rule should remain detectable despite such heterogeneity and should allow early lesion information to forecast patient-specific patterns of distributed GMV loss. At the same time, inter-individual variability in lesion embedding offers an opportunity to examine whether model-derived prediction parameters have interpretable anatomical, topological and molecular correlates.

In this study, we developed and evaluated a lesion-informed connectome diffusion framework for individualized prediction of post-stroke GMV atrophy. Using longitudinal MRI data from two complementary stroke cohorts spanning the hyperacute to chronic stages, we first used CDM to determine which connectome representation provides the most suitable scaffold for modelling distributed atrophy. We then initialized NDM with each patient's lesion map to test whether lesion-informed diffusion captures patient-specific atrophy trajectories. Finally, we examined the biological interpretability of model-derived propagation parameters and tested whether baseline lesion-derived features could support out-of-sample prediction of individualized atrophy patterns without using longitudinal imaging data.

Results

We analysed longitudinal MRI data from a primary cohort[29] (n=72, age: 53.9±10.5 years) and an independent early-phase cohort[30] (n=20, age: 63.3±12.03 years), spanning hyperacute to chronic stages. The primary cohort included imaging at 2 weeks, 3 months, and 12 months post-stroke, enabling characterization of long-term secondary atrophy, whereas the early-phase cohort captured hyperacute structural changes from Day 0/1 to Day 5. Detailed demographic and clinical information for all participants is available in Supplementary Tables 1 and 2.

Structural connectivity provides the scaffold for individualized atrophy modelling

Voxel-wise proportional GMV change maps were computed by comparing follow -up GMV maps with cohort-specific baseline GMV maps after excluding lesion voxels (Fig. 1A). These voxel-wise maps were subsequently parcellated into regional representations using the AICHA atlas[31] and integrated with normative structural and functional connectomes derived from 930 healthy adults from the Human Connectome Project[32] (HCP). Structural connectomes were

constructed using four complementary edge-weighting schemes, including binary adjacency, fractional anisotropy (FA), inverse fibre length (invFL), and fraction of streamlines (FSe), where FSe quantified the proportion of streamlines connecting a region pair relative to the total streamlines extrinsic to those regions[33]. To determine whether post-stroke atrophy follows network constraints and to identify the connectome representation most suitable for subsequent individualized prediction, we applied CDM, which estimates regional GMV change from the weighted GMV changes of network-connected neighbours (Fig.1C).

Across patients, longitudinal GMV changes at 3 and 12 months post-stroke exhibited spatially coordinated patterns extending beyond focal lesion regions. CDM-estimated maps showed strong spatial correspondence with observed GMV changes at both time points (Fig. 1D). CDM performance varied across connectome definitions, with structural connectivity-based models consistently outperforming functional connectivity-based models at both 3 and 12 months (Fig. 1F; structural connectivity, *r* range: 0.26–0.90; functional connectivity, *r* range: -0.02–0.57). Repeated-measures ANOVA confirmed differences across connectome definitions at both time points (both $P < 0.001$). Post hoc paired comparisons showed that functional connectivity yielded lower CDM–observation correspondence than all four structural connectome definitions, whereas FSe-weighted connectomes yielded higher correspondence than all other definitions (FSe-weighted: *r* range: 0.33–0.90; mean *r* [SD] = 0.71 [0.09] at 3 months and 0.69 [0.09] at 12 months). To determine whether CDM performance exceeded that expected under spatial and topological constraints, individual-level correspondence was evaluated against spatial autocorrelation-preserving (SMASH and Spin test[34,35]) and topology-preserving null models (Rewire[36]). Structural connectivity-based models showed robust individual-level performance across both time points, with all patients exceeding null-model thresholds except for one patient at 3 months under the invFL-weighted connectome. In contrast, functional connectivity-based models showed significant CDM–observation correspondence in only 71.0% of patients at 3 months and 54.8% at 12 months. The same overall pattern was replicated under the BNA parcellation (Supplementary Fig. S2A-C).

Applying the same analysis to the early-phase cohort spanning the hyperacute and early acute stages within the first week after stroke revealed a similar overall pattern. Although early GMV changes were more spatially diffuse and less lesion-centred (Supplementary Fig. S3A), structural connectivity-based CDMs again outperformed functional connectivity–based models, with the FSe-weighted connectome yielding the strongest correspondence (*r* range: 0.23–0.77; mean *r* [SD] = 0.50 [0.13]; Supplementary Fig. S3B). Differences across connectome

definitions were again present ($P < 0.001$), with functional connectivity yielding the lowest correspondence overall and FSe-weighted connectomes yielding the highest. Effect sizes were reduced relative to later stages, but structural connectivity constraints were already detectable within the first week after stroke. Together, these findings identify the FSe-weighted structural connectome as the most appropriate anatomical scaffold for lesion-informed modelling of post-stroke atrophy.

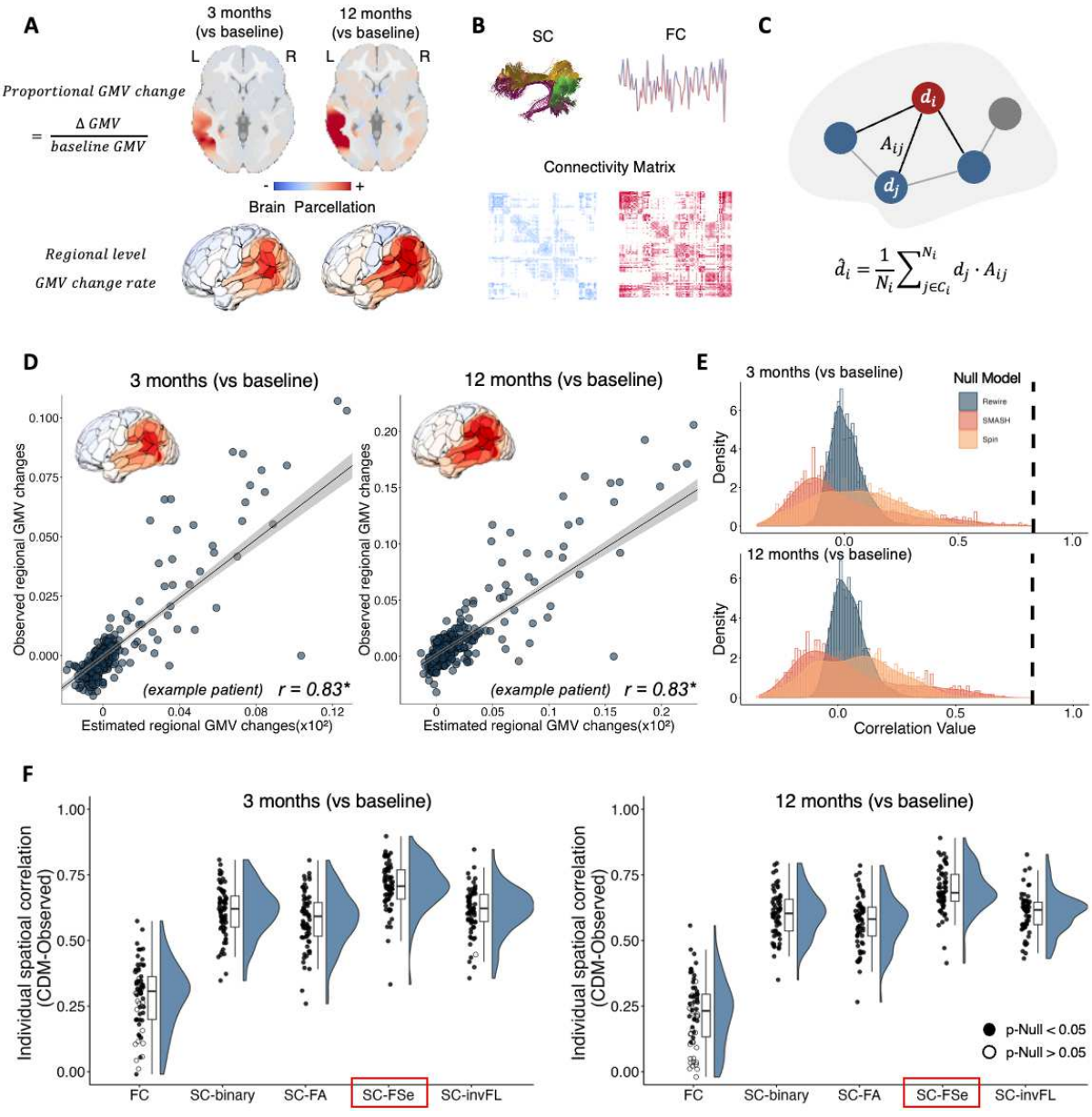

Figure 1. Structural connectivity provides the scaffold for individualized modelling of post-stroke GMV atrophy. (A) Representative patient illustrating individualized proportional GMV change maps (ΔGMV / baseline GMV) at 3 and 12 months post-stroke (baseline ≈ 2 weeks). **(B)** Schematic of structural and functional connectome construction. Structural connectivity (SC) reflects white matter fibre pathways reconstructed from diffusion tractography using multiple edge-weighting schemes, including binary

adjacency, fraction of streamlines (FSe), fractional anisotropy (FA) and inverse fibre length (invFL). Functional connectivity (FC) reflects temporal correlations of resting-state BOLD signals between regions. **(C)** Coordinated deformation model (CDM). Regional GMV change (d_i) is modelled as the weighted aggregation of GMV changes in network-connected regions, scaled by the connectivity strength A_{ij}. **(D)** Representative patient showing correspondence between CDM-estimated and empirically observed regional GMV changes at 3 and 12 months. Each point represents a brain region; lines indicate linear fits. **(E)** Null distributions of CDM-observation correlations generated using spatial autocorrelation-preserving, spin-based, and topology-preserving rewiring procedures. The black dashed line indicates the observed CDM correlation for the representative patient. **(F)** Spatial correlation between CDM-estimated and observed GMV changes across all patients. Filled circles indicate patients whose model performance exceeded all three null models; open circles indicate patients who failed to exceed at least one null model. *$P < 0.05$.

Lesion-informed network diffusion modelling predicts patient-specific atrophy

Building on the identification of structural connectivity as the strongest scaffold for coordinated GMV atrophy, we applied NDM[37,38], which predicts how lesion-initiated atrophy propagates through the structural connectome over time, using the FSe-weighted structural connectome (Fig. 2A-B). Each patient's lesion profile served as the initial condition to generate individualized trajectories of distributed GMV change extending beyond focal lesion sites. Model predictions were compared with empirically observed GMV change patterns across diffusion time, and the maximum correspondence was defined as the NDM prediction accuracy (NDM-PA). An example patient illustrating this workflow is shown in Fig. 2C-E.

Across patients, NDM-PA values were consistently positive at both 3 and 12 months post-stroke (r range: 0.07-0.78; mean r [SD] = 0.47 [0.16] at 3 months; 0.48 [0.17] at 12 months). To evaluate the significance of prediction accuracy, we compared the empirical NDM-PA values with two null model tests, including a SMASH surrogate test and a rewiring test. Under these frameworks, NDM significantly predicted longitudinal GMV alternation patterns in 89.9% of patients at 3 months and 87.1% at 12 months (Fig. 2F). These results were replicated using the BNA parcellation (Supplementary Fig. S2D). Together, these findings indicate that lesion-informed NDM captures patient-specific patterns of longitudinal GMV atrophy.

This pattern was not yet fully expressed in the early-phase dataset within the first week after stroke. At this stage, NDM-PA values were markedly attenuated, and most patients (95%) failed to reach significance (Supplementary Fig. S3C). This contrast suggests that lesion-

initiated, network-consistent atrophy trajectories become progressively organized across subacute and chronic stages rather than being fully established immediately after stroke.

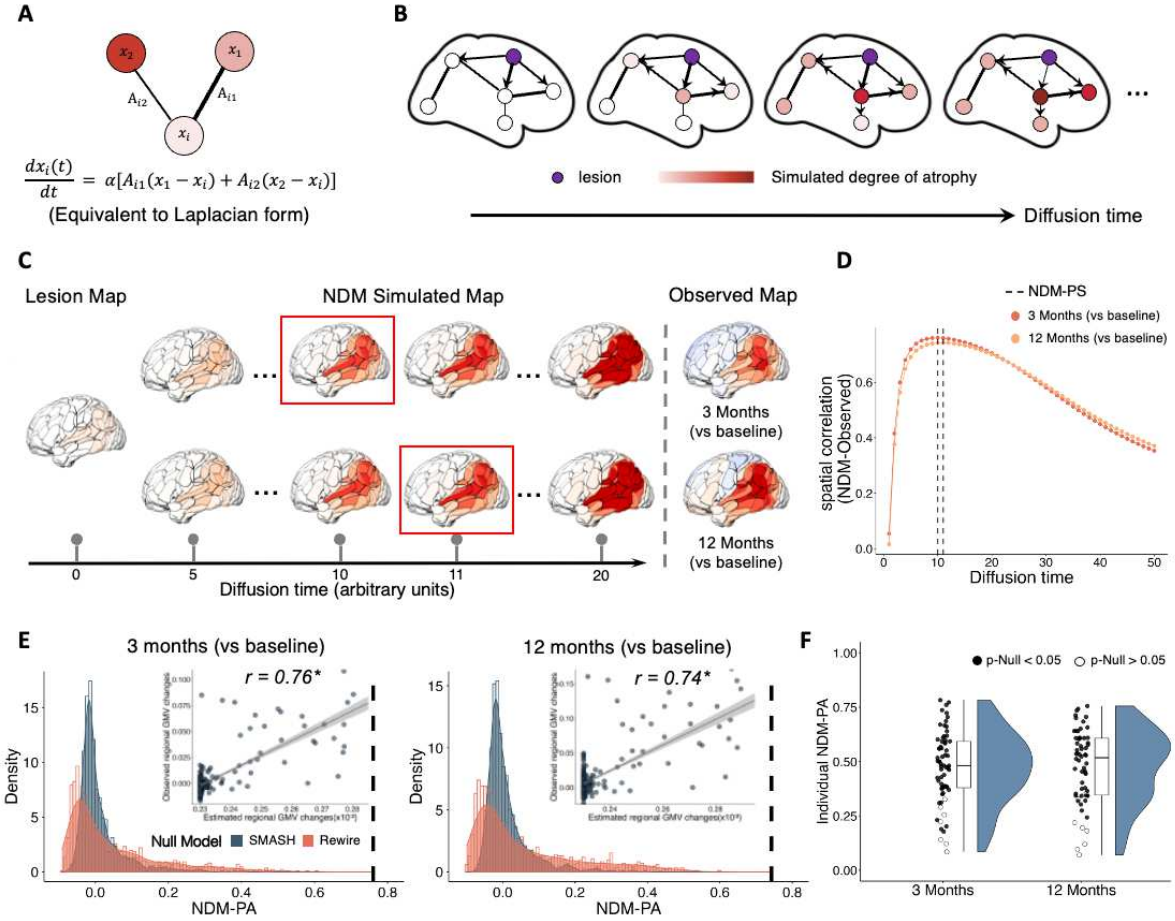

Figure 2. Lesion-informed network diffusion modelling predicts patient-specific GMV atrophy. (A) Network diffusion model describing regional change as a function of weighted differences between each region and its connected neighbours, with coupling strengths defined by the connectivity weight. **(B)** Conceptual illustration of lesion-initiated propagation of pathological load through the structural connectome over diffusion time. Diffusion time is expressed in arbitrary units and does not correspond to chronological time. **(C)** Representative patient illustrating lesion location, network diffusion modelling (NDM)-simulated GMV atrophy maps across diffusion time, and empirically observed GMV atrophy maps at 3 and 12 months post-stroke. For each observation, the NDM-simulated map achieving the highest spatial correlation with the empirical GMV atrophy pattern is highlighted by the red rectangle. **(D)** Spatial correlation between NDM-predicted and observed GMV atrophy maps as a function of diffusion time for the representative patient. The maximum spatial correlation achieved across diffusion time was defined as the NDM prediction accuracy (NDM-PA), and the corresponding diffusion time was defined as the NDM propagation stage (NDM-PS) for that sampling time point. **(E)** Null distributions of NDM-PA generated using spatial autocorrelation-preserving and topology-preserving rewiring procedures. The dashed line indicates the observed NDM-PA for the representative patient. Insets show correspondence between

predicted and observed regional GMV changes at the NDM-PS. **(F)** Distributions of individual NDM-PA values across all patients at 3 and 12 months post-stroke. Filled symbols indicate patients exceeding null thresholds. *$P < 0.05$.

Model-derived propagation stage reveals heterogeneity in atrophy progression

Beyond prediction accuracy, NDM also provides a model-inferred propagation stage (NDM-PS), defined as the diffusion time point at which the simulated atrophy pattern best matches the observed GMV change map. We therefore examined whether NDM-PS could provide a model-derived index of patient-specific atrophy progression beyond chronological time after stroke. If post-stroke atrophy progressed uniformly along the diffusion trajectory, later chronological time points (12 months) would correspond to later NDM-PS within individuals. However, NDM-PS values did not differ between 3 and 12 months at the group level (paired t-test: $t(58) = 0.47$, $P > 0.05$, two-tailed; Fig. 3A). Within-subject shifts in propagation stage (ΔNDM-PS = NDM-PS$_{12\ months}$ − NDM-PS$_{3\ months}$) were broadly distributed around zero (Fig. 3A-B), indicating substantial inter-individual heterogeneity.

We then examined the association between ΔNDM-PS and empirical pattern similarity to determine whether this time–stage dissociation reflects metric instability or meaningful variation in longitudinal atrophy organization. Larger absolute shifts in propagation stage ($|\Delta$NDM-PS$|$) were associated with lower spatial similarity between observed 3- and 12-month GMV change maps (Pearson's $r = -0.73$, $P < 0.001$; Fig. 3C), indicating that variation in NDM-PS corresponds to differences in spatial reorganization of atrophy.

Patients were then stratified according to whether chronological ordering (3 months < 12 months) was concordant with propagation-stage ordering. Twenty subjects exhibited concordant progression (ΔNDM-PS > 0), whereas thirty-nine showed discordant ordering (ΔNDM-PS ≤ 0). As shown in Fig. 3D, the concordant group displayed more spatially extensive or intensified GMV atrophy at 12 months relative to 3 months, whereas the discordant group showed largely overlapping patterns across time. Consistent with this contrast, NDM simulations applied to the incremental 3-to-12-month GMV change map yielded higher NDM-PA in the concordant group than in the discordant group (two-sample t-test: $t(57) = 1.79$, $P < 0.05$, one-tailed; Fig. 3E). These findings suggest that advancement in NDM propagation stage is associated with continued network-consistent atrophy evolution, whereas a substantial subset of patients diverges from diffusion-consistent propagation during the chronic stage.

Validation analyses using the BNA yielded highly comparable overall trends, with the core patterns of atrophy evolution remaining stable across both templates (Supplementary Fig. S4).

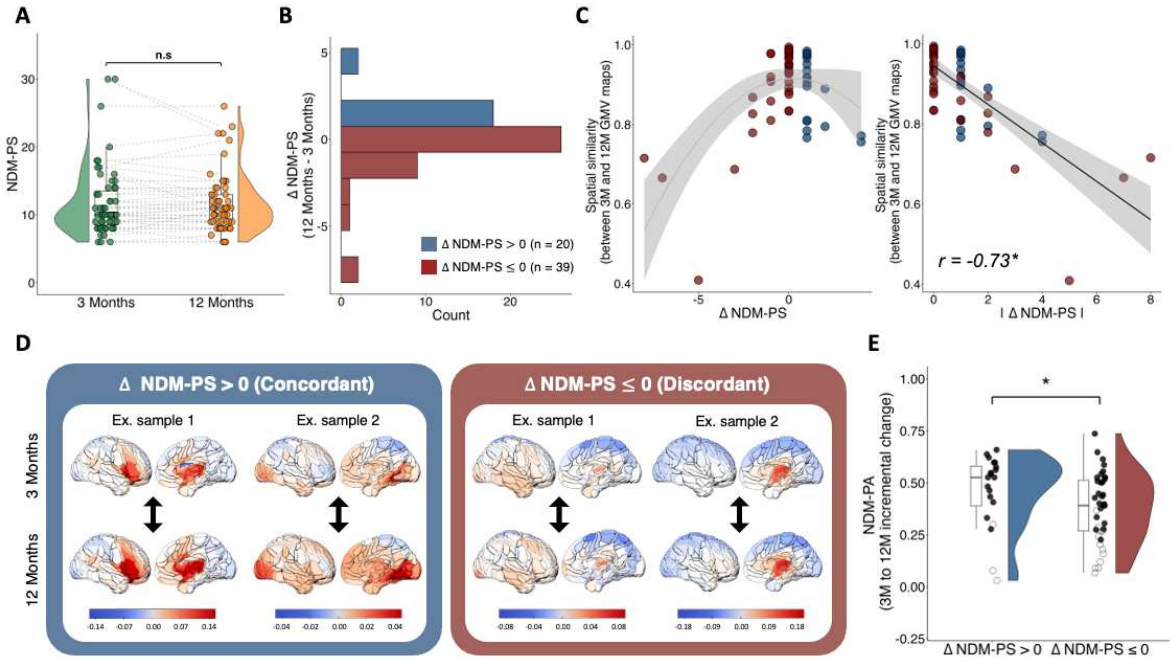

Figure 3. Chronological time after stroke does not consistently track NDM propagation stage. (A) Comparison of NDM propagation stage (NDM-PS) estimated from GMV atrophy patterns at 3 and 12 months post-stroke. (B) Distribution of within-subject differences in propagation stage (ΔNDM-PS = NDM-$PS_{12\ months}$ - NDM-$PS_{3\ months}$). (C) Association between propagation-stage shifts and empirical spatial reorganization of atrophy. Left: spatial similarity between observed 3- and 12-month GMV maps as a function of ΔNDM-PS. Right: larger absolute stage shifts (|ΔNDM-PS|) are associated with lower spatial similarity. (D) Representative examples of patients stratified by chronological-stage ordering concordance (concordant or discordant). (E) NDM prediction accuracy (NDM-PA) for incremental 3-to-12-month GMV change maps for the concordant and discordant patient groups (one-tailed independent sample *t* test). n.s: non-significant, $^{*}P < 0.05$.

Lesion context shapes model-derived propagation stage at 3 months post-stroke

Given the heterogeneous longitudinal shifts in NDM propagation stage observed at 12 months, we focused on the 3-month post-stroke time point, at which NDM-PS remained more comparable across subjects, and examined multi-level lesion-related factors associated with inter-individual variability in NDM-derived parameters.

Neither NDM-PA nor NDM-PS showed significant associations with demographic variables, including age, sex, handedness, and years of education. In contrast, lesion-related factors exhibited clear multi-level associations with NDM parameters.

At the level of lesion topography, we mapped NDM parameters onto lesioned regions and averaged them across subjects with lesions involving each region, revealing marked spatial specificity (Fig. 4A-B). Regions whose lesion involvement was associated with higher mean NDM-PA were concentrated in the left precuneus, posterior cingulate cortex, and superior parietal lobule, indicating that lesions affecting these regions were associated with more predictable atrophy patterns. Regions associated with higher mean NDM-PS included the left parieto-occipital gyrus, right thalamus, and left anterior cingulate cortex, indicating later inferred propagation stages when these regions were involved. Consistent with this spatial heterogeneity, NDM-PS differed significantly across canonical functional systems (Kruskal–Wallis $H = 85.81$, $P < 0.001$), with subcortical and somatomotor systems showing higher propagation stages than other systems, whereas NDM-PA showed no significant between-system differences (Fig. 4C).

At the individual level, global lesion characteristics showed selective associations with NDM parameters. NDM-PA was not significantly related to lesion hemisphere or lesion size. By contrast, NDM-PS decreased with increasing lesion size ($r = -0.32$, $P_{FDR} < 0.05$), indicating that larger lesions were associated with less advanced propagation stages at 3 months (Fig. 4D).

The network-topological and molecular properties of lesioned regions were also differentially related to NDM parameters. NDM-PA showed no significant associations with lesion-site topological or molecular features. In contrast, NDM-PS exhibited a broader association pattern: longer propagation stages were associated with higher betweenness centrality of lesioned regions ($r = 0.42$, $P_{FDR} < 0.05$), whereas shorter propagation stages were associated with higher local clustering coefficient ($r = -0.43$, $P_{FDR} < 0.05$) (Fig. 4E). At the molecular level, NDM-PS was additionally associated with neurotransmitter receptor/transporter profiles of lesioned regions, with the strongest effect observed for the 5-HT2a receptor ($r = -0.42$, $P_{FDR} < 0.05$) (Fig. 4F). Together, these findings indicate that the model-derived propagation stage is biologically interpretable and is shaped by lesion topography, lesion size, and the network-topological and molecular context of the damaged region, whereas NDM prediction accuracy is comparatively less sensitive to these subject-level determinants. Results were broadly consistent under the BNA parcellation, supporting the robustness of these associations across atlas definitions (Supplementary Fig. S5).

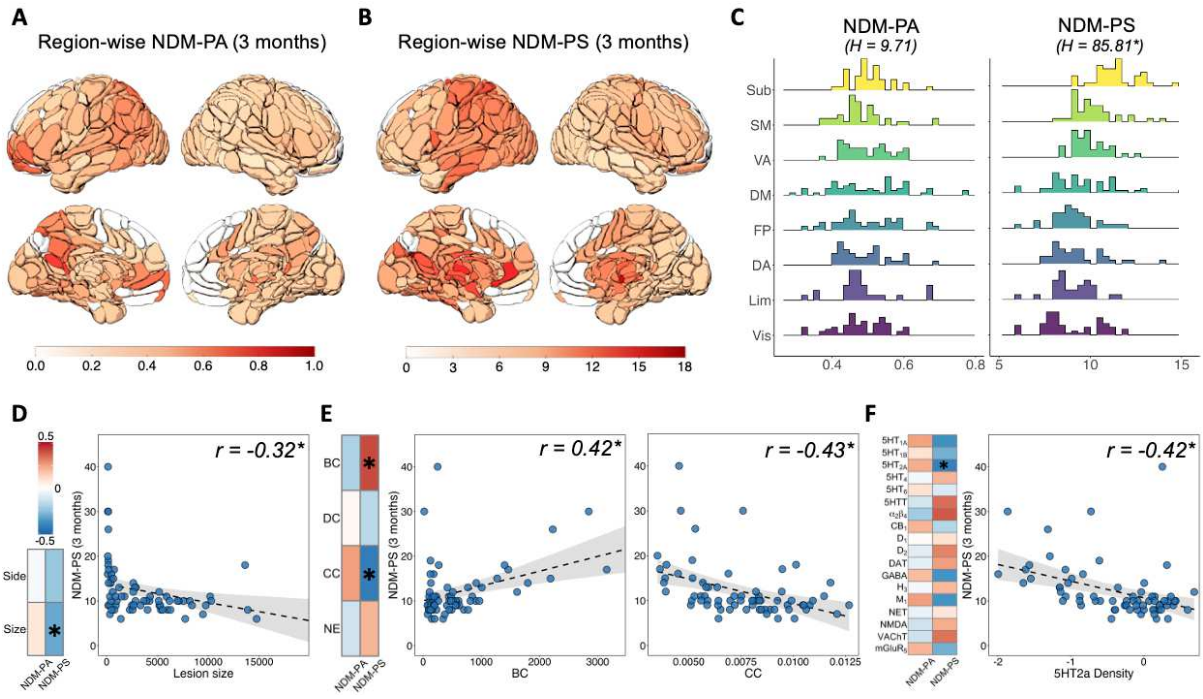

Figure 4. Multi-level lesion-related associations of NDM parameters at 3 months post-stroke. (A) Region-wise map of NDM-PA at 3 months post-stroke. Values indicate the mean NDM-PA across subjects with lesions involving the corresponding region. **(B)** Region-wise map of NDM-PS at 3 months post-stroke. Values indicate the mean NDM-PS across subjects with lesions involving the corresponding region. **(C)** Distribution of region-wise NDM-PA and NDM-PS across the seven Yeo functional networks and a subcortical system. NDM-PS differed significantly across systems (Kruskal–Wallis test: $H = 85.81$, $P < 0.001$), whereas NDM-PA did not ($H = 9.71$, $P > 0.05$). Vis, visual; SM, somatomotor; DA, dorsal attention; VA, ventral attention; Lim, limbic; FP, frontoparietal; DM, default mode; Sub, subcortical. (D-F) Subject-level associations of NDM-PA and NDM-PS with lesion-related factors. Heatmaps show Pearson correlation coefficients, and scatterplots show associations surviving permutation-based false discovery rate correction. Dashed lines and shaded bands indicate linear fits and 95% confidence intervals. Asterisks indicate associations surviving FDR correction ($P_{FDR} < 0.05$). **(D)** Subject-level associations of NDM-PA and NDM-PS with global lesion characteristics, including lesion side and lesion size. **(E)** Subject-level associations of NDM-PA and NDM-PS with network-topological properties of lesioned regions, including betweenness centrality (BC), degree centrality (DC), clustering coefficient (CC), and nodal efficiency (NE). **(F)** Subject-level associations of NDM-PA and NDM-PS with neurotransmitter receptor/transporter profiles of lesioned regions derived from PET maps.

Baseline lesion information enables out-of-sample forecasting of individualized GMV atrophy

We next asked whether baseline lesion information alone is sufficient to forecast individualized GMV atrophy patterns within the NDM framework. Whereas the preceding analyses derived

NDM-PS by aligning simulated diffusion trajectories to observed longitudinal GMV atrophy patterns, here we predicted NDM-PS out of sample by training a regression model on input features extracted from baseline lesion maps under leave-one-out cross-validation (Fig. 5A–B). The predicted NDM-PS was then used to sample the lesion-initiated NDM trajectory for each patient and generate individualized GMV atrophy forecasts.

Across participants, regression-predicted NDM-PS values were significantly correlated with empirically derived NDM-PS values obtained by aligning NDM simulations to observed longitudinal GMV atrophy patterns ($r = 0.31$, $P < 0.001$; Fig. 5C), exceeding permutation-based null expectations. Consistent with the observed association between lesion context and NDM-PS, this result suggests that baseline lesion patterns carry predictive information about patient-specific diffusion staging. Using the predicted NDM-PS values, out-of-sample GMV atrophy forecasts showed spatial correspondence with observed longitudinal GMV changes. At the group level, this correspondence was comparable to those generated using empirically derived NDM-PS values (Fig. 5D). Similar predictive performance was observed under the BNA parcellation (Supplementary Fig. S6).

Together, these findings suggest that lesion-informed estimation of NDM propagation stage enables out-of-sample prediction of individualized GMV atrophy patterns without requiring longitudinal imaging data as model input.

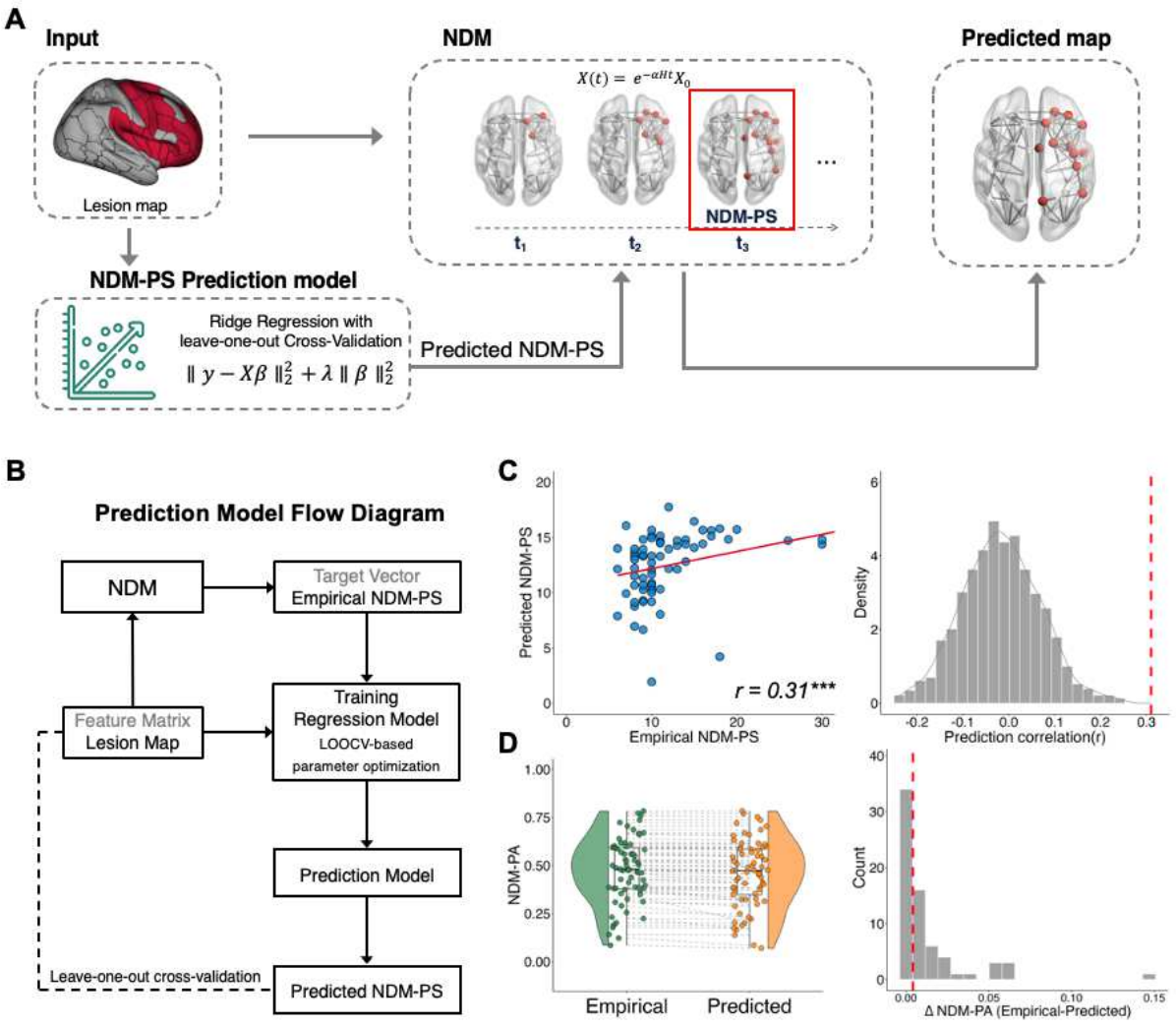

Figure 5. Lesion-informed NDM enables out-of-sample prediction of individualized GMV atrophy. (A) Framework for individualized prediction of GMV atrophy patterns. Lesion maps serve as input to NDM to generate time-resolved simulated GMV change maps. A ridge regression model with leave-one-out cross-validation is trained to predict subject-specific NDM-PS from lesion-derived features. The predicted NDM-PS is then used to select the corresponding NDM-simulated GMV map for each individual. **(B)** Flow diagram of the prediction procedure. Lesion-derived regional features are used to train a regression model to estimate empirical NDM-PS values. The trained model generates out-of-sample predicted NDM-PS for each subject, which are subsequently input to NDM to produce individualized GMV atrophy predictions. **(C)** Prediction accuracy of NDM-PS. Left: correlation between predicted and empirically derived NDM-PS values across individuals. Right: null distribution of prediction correlations obtained from permutation testing; the dashed line indicates the observed prediction performance. **(D)** Spatial correspondence between observed GMV atrophy patterns and NDM predictions generated using empirically derived NDM-PS versus regression-predicted NDM-PS. Group-level distributions of NDM-PA demonstrate comparable spatial performance between the two approaches. The right panel shows the distribution of differences in NDM-PA between empirical-stage and predicted-stage models. ***$P < 0.001$.

Discussion

We present a lesion-informed connectome diffusion framework for individualized prediction of distributed brain atrophy after stroke. By combining longitudinal MRI, normative structural connectomics, graph-based diffusion modelling and cross-validated prediction, the framework transforms each patient's lesion map into an interpretable whole-brain change trajectory. Across two complementary stroke cohorts spanning the hyperacute to chronic stages, structural connectivity provided the dominant scaffold for modelling distributed GMV atrophy; lesion-initialized NDM captured patient-specific atrophy patterns at 3 and 12 months; model-derived propagation stage varied with lesion topology and molecular context; and baseline lesion features supported out-of-sample prediction of individualized atrophy maps. These findings shift the study of post-stroke degeneration from descriptive mapping of remote atrophy toward a computational framework for forecasting patient-specific structural consequences of focal brain injury.

Our results identified the structural connectome as the dominant anatomical scaffold for individualized modelling of post-stroke degeneration. CDM analyses showed that regions tended to exhibit coordinated GMV loss with their structurally connected neighbours, and that this dependence was already detectable in the hyperacute stage before becoming more pronounced over time. By contrast, functional connectivity provided a much weaker account of coordinated change. This contrast suggests that the large-scale organization of remote degeneration is anchored less in transient functional coupling[39–41] than in the relatively stable anatomical pathways[42] through which lesion effects are embedded and distributed[43,44]. In this respect, the coordinated decline observed via CDM may reflect biological processes mediated by the underlying white matter, whereby Wallerian degeneration and inflammatory signalling propagate through anatomical links to synchronize structural loss across connected regions[45–49]. For the present framework, this result establishes why a structural, rather than functional, connectome should serve as the primary substrate for lesion-informed prediction.

The superior performance of the FSe-weighted connectome underscores this point further. Binary connection presence alone, as well as weights derived from path length or microstructural metrics, proved less predictive than a representation that also captured the relative strength or capacity of anatomical projections[33]. This suggests that what matters is not merely the existence or distance of a pathway, but the degree to which a region is embedded within the white matter architecture that scales the transmission of lesion effects[50]. More

broadly, this finding indicates that network models of post-stroke degeneration should be sensitive not simply to topology, but to graded differences in the capacity of structural pathways to support coordinated downstream change.

NDM extends this structural scaffold into a patient-specific generative model. When initialized with each patient's lesion map, NDM generated simulated atrophy patterns that significantly corresponded to observed GMV changes at both 3 and 12 months post-stroke. Under this framework, post-stroke structural reorganization can be conceptualized as a network-mediated process in which lesion location serves as an individualized initial condition, and subsequent changes emerge over time as a function of each region's structural coupling to affected regions[37,38]. The simulated dynamics of the NDM may find a plausible biological basis in transneuronal degeneration, a potential driver of secondary decay where neurons undergo deterioration following the loss of afferent input or trophic support[51–55]. Such an interpretation is supported by prior observations that regions structurally connected to the lesion are more likely to exhibit subsequent atrophy[13,50,56]. Under this view, the diffusion-like behaviour captured by NDM is best interpreted not as literal spread of pathogenic agents, but as a compact model for predicting how lesion-induced vulnerability is distributed across structurally connected region after focal injury.

The contrast between early-acute and later-stage NDM results further clarifies when this prediction framework becomes informative. Model performance remained limited in the early-acute stage, even though structural network constraint was already detectable with CDM. This divergence suggests that early network dependence and subsequent network-consistent propagation are related but not identical features of post-stroke degeneration. One implication is that focal injury may first establish the conditions for distributed vulnerability, whereas the transneuronal cascades approximated by the NDM require weeks or months to manifest, ultimately driving a diffusion-like pattern of macroscopic volume loss[15,57–60]. The present NDM should therefore be viewed as distilling one dominant organizing principle of later degeneration, rather than an exhaustive account of the diverse pathophysiological processes present across the entire post-stroke time course[61–63].

This perspective also helps clarify the meaning of NDM-derived propagation stage in the context of individualized forecasting. The present results suggest that propagation stage should not be treated as a simple proxy for chronological time after stroke. Although NDM captured atrophy patterns at both 3 and 12 months, inferred propagation stage did not increase monotonically across individuals. Instead, it reflects the topological depth of the diffusive

progression, marking the specific point in the simulated diffusion process where network-mediated patterns best align with empirical observations. At the group level, the limited advancement from 3 to 12 months raises the possibility that the major topographic organization of secondary degeneration is established relatively early, supported by the high spatial stability of atrophy patterns observed between these sessions. This stagnation likely reflects a plateau in the subacute-to-chronic transition, where the neural plasticity or intrinsic resistance mechanisms emerge to counteract further pathological propagation[59,64,65]. NDM propagation stage is therefore better characterized as a model-derived state variable that summarizes where an individual observed atrophy pattern falls along a network-consistent diffusion trajectory, rather than as a literal measure of elapsed biological time.

The factors associated with variation in this state variable reinforce the interpretability of the framework. Inter-individual variation in propagation stage was related primarily to lesion-related features rather than demographic variables. Larger lesions were associated with shorter inferred propagation stages, whereas lesions involving regions with high betweenness centrality or low local clustering showed patterns suggestive of broader network involvement. This aligns with a "targeted attacks" framework, where damage to highly central elements disproportionately perturbs large-scale organization[66,67]. Furthermore, propagation stage was significantly associated with the 5-HT2a and 5-HT1a receptor density of the lesioned regions. These molecular associations are biologically plausible given convergent evidence that serotonergic signalling—particularly 5-HT1a—is implicated in neuroprotection, post-ischaemic plasticity and functional recovery[68,69], whereas 5-HT2a-related variation has also been associated with ischaemic stroke susceptibility, potentially through serotonergic effects on vascular contraction and platelet aggregation[70]. Collectively, these observations suggest that the forecasted trajectory of distributed atrophy depends on where a lesion sits within the brain's integrated topological and molecular landscape[13,56,71].

The lesion-informed prediction results highlight the translational potential of this modelling framework. Although prior work has shown that lesion-induced connectivity disruption can predict future tissue loss at the group level[13], the proposed workflow uses early lesion information to estimate patient-specific propagation stage and generate forecasts of longitudinal GMV atrophy through the structural connectome. By incorporating NDM, the prediction shifts from local damage alone to lesion embedding within a network model of secondary degeneration. Although still a proof of concept, this predictive mapping could facilitate patient stratification by identifying individuals most susceptible to widespread

neurodegeneration. The methodology offers a clinically relevant strategy for anticipating individual patterns of remote structural change, thereby informing future monitoring, neuroprotective intervention or rehabilitation planning before such changes become consolidated[72–75].

A few limitations warrant consideration. First, while the NDM effectively captures network-mediated atrophy, its simplified framework does not model concurrent neuroplastic remodelling or compensatory hypertrophy, suggesting the need for more biologically nuanced models in future studies. Second, the current study used normative connectomes as a reference; future work with patient-specific network data may refine atrophy mapping and clarify how direct network alterations relate to structural decay. Although the normative functional connectome showed limited explanatory power for coordinated GMV loss here, directly measured patient functional connectomes may perform better for modelling recovery-related processes[76,77]. Finally, linking NDM-predicted atrophy to specific clinical deficits, treatment response and rehabilitation outcomes remains a crucial next step for establishing the translational utility of this framework.

In conclusion, this study establishes a lesion-informed connectome diffusion framework for individualized prediction of post-stroke brain atrophy. By using early lesion information to initialize a structural-network model, the framework captures patient-specific patterns of remote degeneration, yields biologically interpretable propagation parameters and provides a basis for forecasting later whole-brain structural reorganization after stroke.

Methods

Participants and datasets

We analysed a longitudinal stroke cohort[29] comprising 132 patients (age range, 19–83 years) with first-ever symptomatic infarction. Participants were not selected on the basis of lesion location, vascular territory, or behavioural phenotype, thereby preserving broad clinical representativeness. Structural MRI was acquired at approximately 2 weeks (acute baseline), 3 months (subacute stage), and 12 months (chronic stage) post-stroke.

Using previously reported quality-control procedures[78], we excluded eight participants because of suboptimal T1-weighted image quality. Patients with isolated infratentorial lesions were additionally excluded, restricting analyses to cortical and subcortical grey matter change. The

final analytical sample comprised 72 patients with high-quality baseline structural imaging and at least one follow-up structural scan (72 at baseline, 69 at 3 months, 62 at 12 months). Demographic and clinical characteristics are summarised in Supplementary Table 1.

We also analysed an independent early-phase cohort (n = 28) from a previously published dataset,[30] which provided coverage of the first week after stroke onset and complemented the main longitudinal cohort beginning at approximately 2 weeks post-stroke. MRI was acquired at Day 0 (<24 h), Day 1 (24–48 h), and Day 5 (4–6 days; mean ± SD = 4.93 ± 0.38 days). Given that volumetric alterations within the first 24–48 hours are expected to be modest relative to measurement variability, analyses focused on the contrast between the combined Day 0/Day 1 scans and the Day 5 scan. After quality control, 20 patients with complete longitudinal data were retained (Supplementary Table 2).

MRI acquisition

All stroke participants underwent MRI scanning on 3T scanners. Acquisition parameters for both stroke cohorts are provided in the Supplementary Materials.

Lesion segmentation

For the primary longitudinal cohort, T1-weighted MPRAGE images were used for grey matter volume (GMV) estimation, whereas lesion identification was based on multimodal structural images (T1, T2, and FLAIR). Lesions were manually segmented in native space from baseline structural images acquired within 2 weeks post-stroke using Analyze biomedical imaging software[79]. All segmentations were reviewed by an experienced neurologist to verify lesion boundaries and lacunar involvement. Lesion masks were subsequently normalized to MNI space using previously established gradient-alignment and atlas-transformation protocols[80].

For the early-phase cohort, lesions were manually delineated on Day 0 diffusion-weighted images. Masks were drawn by one investigator and independently verified by a second stroke imaging specialist. Lesion masks were then normalized to MNI space and dilated by one voxel (3×3×3 kernel) using FSL to mitigate potential registration mismatch[81]. Processing scripts for this cohort are publicly available.

Longitudinal voxel-based morphometry

Longitudinal structural changes were assessed using the longitudinal VBM toolbox implemented in SPM12 (http://www.fil.ion.ucl.ac.uk/spm). For each participant, an unbiased within-subject average image was generated using the Serial Longitudinal Registration toolbox[82]. The average images were bias-corrected and segmented into grey matter, white matter, and cerebrospinal fluid probability maps, and subsequently normalized to MNI space.

Stroke lesions were masked during segmentation and spatial normalization to prevent tissue misclassification[83]. GM maps were modulated using Jacobian determinants derived from both native-to-average and average-to-MNI transformations to preserve volumetric information. The resulting GMV maps were smoothed using an 8-mm full-width-at-half-maximum Gaussian kernel and restricted to grey matter using a high-resolution GM mask derived from the Human Connectome Project. All preprocessing steps underwent visual quality control.

Spatial mapping of longitudinal GMV change

After generating whole-brain voxel-wise GMV maps for all available time points, lesion voxels were masked out from each GMV map prior to longitudinal change estimation. Longitudinal GMV change was quantified at the individual level relative to a cohort-specific baseline. For the primary longitudinal cohort, the 2-week scan served as baseline and proportional GMV change was calculated for the 3- and 12-month scans. For the early-phase cohort, the combined Day 0/Day 1 scan served as baseline and proportional GMV change was calculated for Day 5. Proportional GMV change was defined as follows:

$$\Delta GMV = \frac{GMV_{\text{followup}} - GMV_{\text{baseline}}}{GMV_{\text{baseline}}} \quad (1)$$

This normalization reduces potential confounding arising from regional differences in baseline GMV magnitude and is widely used in longitudinal morphometric studies of neurodegeneration and brain injury[84,85].

Voxel-wise GMV change maps were parcellated into 384 cortical and subcortical regions using the Atlas of Intrinsic Connectivity of Homotopic Areas (AICHA) [31], enabling integration with connectome-based modelling. Regional GMV change was computed as the mean proportional change across all constituent voxels, yielding a 384 × 1 regional GMV change vector for each

subject and each time interval. All analyses were also replicated using the Brainnetome Atlas (BNA) [86], and the corresponding validation results are reported in the Supplementary Materials.

Normative connectome construction

Normative connectomes were derived from 930 healthy adult participants from the HCP young adult cohort, providing a reference independent of our stroke corhorts[32]. The architecture of resulting networks are visualised in Supplementary Fig. 1.

Normative structural and functional connectomes were estimated from diffusion-weighted imaging and resting-state functional MRI data. All imaging data were processed using the standardized HCP minimal preprocessing pipelines[87], with additional denoising and quality-control procedures described in the Supplementary Materials. The resulting connectomes served as cohort-independent normative references for all connectome-based modelling analyses.

Whole-brain probabilistic tractography with anatomical constraints was performed to construct the structural connectome. The AICHA and BNA atlases were aligned to individual native diffusion space, and streamlines were assigned to region pairs based on the proximity of their endpoints to the parcellated regions. Four edge-weighting schemes were examined: binary adjacency, fractional anisotropy (FA), inverse fibre length (invFL), and fraction of streamlines (FSe). FSe was defined as the proportion of streamlines connecting two regions relative to the total number of streamlines extrinsic to those regions[33,88]. Edges that were not reliably present across participants were excluded to reduce the influence of potentially spurious tractography-derived connections. The remaining individual weighted connectivity matrices were then averaged across participants to generate the group-level normative structural connectome.

The same AICHA and BNA atlases were used to define regional nodes, ensuring direct comparability with the structural connectome. Representative time series were extracted by averaging voxel-wise signals within each region. Functional connectivity was quantified using Pearson correlation between regional time series and subsequently Fisher z-transformed. Individual functional connectivity matrices were averaged across participants to generate the group-level normative functional connectome.

Coordinated deformation modelling to identify connectome constraints for atrophy prediction

We employed coordinated deformation modelling (CDM) to test whether longitudinal GMV change after stroke is constrained by brain network architecture, thereby identifying the connectome representation most suitable for subsequent individualized prediction. CDM was originally developed to examine whether patterns of structural deformation align with underlying connectivity structure[21]. The model assumes that regional structural change reflects coordinated influences from network-connected regions, rather than independent or purely local processes.

Within this framework, the GMV change of each region was modelled as a weighted aggregation of GMV changes in its network neighbours, where weights correspond to inter-regional connectivity strength (Fig. 1C). CDM has previously been applied to neurodegenerative and psychiatric conditions to evaluate whether spatial patterns of group-level atrophy conform to network constraints[26,89,90], but it has not been systematically examined in focal brain lesions with longitudinal individual-level data.

Formally, for each region *i*, the estimated GMV change $\widehat{d_i}$ was defined as:

$$d_i = \frac{1}{N_i} \sum_{j \in C_i}^{N_i} d_j \bullet A_{ij} \qquad (2)$$

where d_j denotes the observed GMV change in region j, A_{ij} represents the connectivity strength between regions i and j, C_i denotes the set of regions connected to i, and N_i is the number of such connections.

CDMs were constructed using both structural and functional connectomes under multiple weighting schemes. For each subject, CDM-derived GMV change maps were compared with empirically observed maps across all available longitudinal intervals. These included the 2-week-to-3-month and 2-week-to-12-month intervals in the primary longitudinal cohort and the first week after stroke in the independent early-phase cohort. Model performance was quantified using Pearson correlation, with statistical significance assessed using spatial and network-based null models.

To determine which connectome definition best captured coordinated post-stroke GMV change across regions, we compared CDM performance across the five connectome definitions at the

group level using a one-way repeated-measures ANOVA. Significant main effects were followed by Bonferroni-corrected post hoc paired t-tests.

Lesion-informed network diffusion modelling

To generate individualized predictions of post-stroke GMV change, we implemented network diffusion modelling (NDM)[37,38], a generative graph-based framework for simulating network-constrained pathological propagation from a patient-specific lesion map (Fig. 2A-B). NDM formalizes pathological spread as a first-order diffusion process on the graph Laplacian of a connectivity matrix. The evolution of the regional pathological state vector $X(t)$ is governed by:

$$\frac{dX(t)}{dt} = -\alpha HX(t) \quad (3)$$

where $X(t)$ represents the simulated pathological load across regions at diffusion time t, H represents the graph Laplacian of the normative connectivity matrix, and α is a global diffusion rate parameter fixed to 1 for all subjects.

The closed-form solution is:

$$X(t) = e^{-\alpha Ht} X_0 \quad (4)$$

where X_0 specifies the initial pathological state. For each patient, the voxel-wise lesion mask was mapped onto the atlas parcellation and converted into a regional binary lesion vector, with regions overlapping the lesion mask assigned a value of 1 and all remaining regions assigned a value of 0. The binary lesion vector served as X_0, allowing each patient's focal lesion to initialize the model and generate a personalized whole-brain diffusion trajectory through the structural connectome.

For each subject, NDM simulations were performed across a continuous diffusion-time interval ($t \in [0,50]$), sufficient to capture the full range of propagation dynamics (Fig. 2C). At each diffusion time point, the simulated GMV change pattern was compared with the empirically observed GMV change map using Pearson correlation (Fig. 2D). The maximum correlation value across diffusion time was defined as the NDM prediction accuracy (NDM-PA), and the statistical significance of the NDM-PA value was evaluated using spatial null models (Fig. 2E).

The diffusion time at which this maximum correlation was achieved corresponds to the model-inferred propagation stage that best matches the observed GMV change pattern. This time point was defined as the NDM propagation stage (NDM-PS) for that sampling time point post-stroke.

Null models

Multiple complementary null models were implemented to determine whether CDM or NDM performance exceeded that expected under spatial and topological constraints.

Spatial autocorrelation-preserving surrogate maps were generated using the BrainSMASH framework,[34,91] which retains the empirical spatial autocorrelation structure while permuting regional values. In addition, spin-based nulls were applied to control for cortical spatial embedding.[35,91] Intrinsic network topology was addressed through degree-preserving random rewiring implemented in the Brain Connectivity Toolbox,[36] generating topology-matched surrogate connectomes.

CDM analyses incorporated spatial autocorrelation-preserving, spin-based, and topology-preserving nulls, whereas NDM analyses utilized spatial autocorrelation and topology-preserving nulls. Detailed implementation procedures are provided in the Supplementary Materials.

Within-subject comparison of chronological time and NDM propagation stage

The relationship between chronological progression after stroke and model-inferred propagation stage was examined by comparing NDM-PS values derived from GMV change patterns at 3 and 12 months within subjects with complete longitudinal imaging. Group-level differences in NDM-PS between the two time points were assessed using paired t-tests. Within-subject changes were quantified as $\Delta\text{NDM-PS} = \text{NDM-PS}_{12\text{ months}} - \text{NDM-PS}_{3\text{ months}}$.

This longitudinal quantification enabled the stratification of subjects according to whether chronological ordering from 3 to 12 months was concordant with diffusion stage: subjects exhibiting an increase in propagation stage over chronological time were defined as the concordant group ($\text{NDM-PS}_{12\text{ months}} > \text{NDM-PS}_{3\text{ months}}$), whereas the others were classified as the discordant group ($\text{NDM-PS}_{12\text{ months}} \leq \text{NDM-PS}_{3\text{ months}}$).

Spatial similarity between 3 and 12-month GMV change maps was quantified using Pearson correlation. In addition, an interval-specific GMV change map (3-to-12 months) was constructed for each subject to characterize incremental structural change during the chronic stage. NDM simulations were further applied to these incremental GMV change maps, and NDM-PA was compared between concordant and discordant groups.

Multi-level correlates of NDM parameters

Following the observation of heterogeneous longitudinal propagation-stage shifts at 12 months, analyses of inter-individual correlates of NDM-derived parameters were conducted at the 3-month post-stroke time point, at which propagation-stage estimates remained more comparable across subjects.

We first examined whether demographic variables, including age, sex, handedness, and years of education, were associated with NDM-PA and NDM-PS. We then examined lesion-related effects across multiple levels, including lesion topography, global lesion characteristics, and the network-topological and molecular properties of lesioned regions. At the regional level, individual NDM parameters were mapped onto lesioned regions defined by the AICHA and BNA atlases and averaged across subjects with lesions involving each region, generating region-wise NDM-PA and NDM-PS maps. Regions with higher mean NDM-PA or NDM-PS indicated locations where lesion involvement was associated with better NDM performance or later inferred propagation stage, respectively. System-level effects were assessed by assigning region-wise NDM parameter maps to canonical functional systems and testing for between-system differences in parameter values. Between-system differences were evaluated using a Kruskal–Wallis test[92], followed by Bonferroni-corrected two-sided Mann–Whitney U tests for pairwise post hoc comparisons[93,94].

At the subject level, lesion hemisphere and lesion volume were tested for associations with NDM-PA and NDM-PS across subjects. To evaluate the role of lesion-site network topology, nodal properties of AICHA- and BNA-defined regions—including degree centrality, betweenness centrality, local clustering coefficient, and nodal efficiency—were derived from the normative structural connectome above. Subject-specific topological features were obtained by averaging these nodal metrics across all lesioned regions and were then tested for associations with NDM-PA and NDM-PS across subjects. In addition, to assess the contribution of the molecular environment of lesioned regions, neurotransmitter receptor and

transporter density maps were obtained using the neuromaps toolbox[95,96]. For each subject, receptor/transporter densities were averaged across all lesioned regions to generate subject-specific molecular profiles, and their associations with NDM-PA and NDM-PS were evaluated across subjects. Statistical significance for all subject-level associations was determined using permutation tests by shuffling the NDM metrics across subjects to generate null distributions[97]. The resulting p-values were then corrected for multiple comparisons within each analysis category using the false discovery rate (FDR) method, with significance set at $P_{FDR} < 0.05$[98].

Lesion-informed prediction of individualized GMV atrophy patterns

Building on the NDM framework described above, we developed a forecasting procedure to predict individualized GMV atrophy patterns from baseline lesion information alone. A schematic overview of this predictive workflow is presented in Fig. 5A.

Ridge regression was used to estimate subject-specific NDM propagation stage (NDM-PS) from lesion-derived spatial features (Fig. 5B)[99]. L2 regularization was applied to stabilize parameter estimation in the high-dimensional feature space. Model training and evaluation were conducted using a nested leave-one-out cross-validation framework, in which one subject was held out for testing in each outer fold and the remaining subjects were used for training. An inner cross-validation loop was used to optimize the regularization parameter[100].

Predicted NDM-PS values were incorporated into NDM to generate individualized simulated GMV atrophy maps. Prediction performance was quantified as the spatial correlation between simulated and empirically observed GMV atrophy patterns, providing a direct assessment of whether early lesion information can forecast later distributed atrophy. Statistical significance was evaluated using permutation testing within the cross-validation framework[101].

This procedure enabled evaluation of whether lesion-informed NDM-PS estimation supports individualized prediction of longitudinal structural degeneration patterns without requiring longitudinal imaging data as input.

Data availability

The data supporting the findings of this study are derived from two primary sources. The main longitudinal cohort data are publicly accessible through the Central Neuroimaging Data Archives (CNDA) at https://cnda.wustl.edu/ under the reference number CCIR_00299. For the early-phase cohort, data are not publicly available due to institutional restrictions and data ownership agreements; however, data may be made available from authors upon reasonable request, subject to a formal data use agreement and institutional approval.

Competing interests

The authors report no competing interests.

Supplementary material

Supplementary information is available online.

References

1. Egorova-Brumley N, Khlif MS, Werden E, Bird LJ, Brodtmann A. Grey and white matter atrophy 1 year after stroke aphasia. *Brain Commun*. 2022;4(2):fcac061. doi:10.1093/braincomms/fcac061

2. Newman-Norlund RD, Gibson M, Johnson L, et al. Cerebellar Atrophy and Language Processing in Chronic Left-Hemisphere Stroke. *Neurobiol Lang*. 2024;5(3):722-735. doi:10.1162/nol_a_00120

3. Thiel A, Vahdat S. Structural and Resting-State Brain Connectivity of Motor Networks After Stroke. *Stroke*. 2015;46(1):296-301. doi:10.1161/STROKEAHA.114.006307

4. Diao Q, Liu J, Wang C, et al. Gray matter volume changes in chronic subcortical stroke: A cross-sectional study. *NeuroImage Clin*. 2017;14:679-684. doi:10.1016/j.nicl.2017.01.031

5. Falcao ALE, Reutens DC, Markus R, et al. The resistance to ischemia of white and gray matter after stroke. *Ann Neurol*. 2004;56(5):695-701. doi:10.1002/ana.20265

6. Sachdev PS, Chen X, Joscelyne A, Wen W, Altendorf A, Brodaty H. Hippocampal size and dementia in stroke patients: The Sydney stroke study. *J Neurol Sci*. 2007;260(1-2):71-77. doi:10.1016/j.jns.2007.04.006

7. Van Niftrik CHB, Visser TF, Sebök M, et al. Delayed cerebral atrophy after cerebellar stroke: topographical relation and clinical impact. *Brain Commun*. 2021;3(4):fcab279. doi:10.1093/braincomms/fcab279

8. Werden E, Cumming T, Li Q, et al. Structural MRI markers of brain aging early after ischemic stroke. *Neurology*. 2017;89(2):116-124. doi:10.1212/WNL.0000000000004086

9. Iadecola C, Buckwalter MS, Anrather J. Immune responses to stroke: mechanisms, modulation, and therapeutic potential. *J Clin Invest*. 2020;130(6):2777-2788. doi:10.1172/JCI135530

10. Okar SV, Topcuoglu MA, Yemisci M, Cakir Aktas C, Oguz KK, Arsava EM. Post-stroke inflammatory response is linked to volume loss in the contralateral hemisphere. *J Neuroimmunol*. 2020;344:577247. doi:10.1016/j.jneuroim.2020.577247

11. Zhao Y, Zhang X, Chen X, Wei Y. Neuronal injuries in cerebral infarction and ischemic stroke: From mechanisms to treatment (Review). *Int J Mol Med*. 2021;49(2):15. doi:10.3892/ijmm.2021.5070

12. Duering M, Righart R, Csanadi E, et al. Incident subcortical infarcts induce focal thinning in connected cortical regions. *Neurology*. 2012;79(20):2025-2028. doi:10.1212/WNL.0b013e3182749f39

13. Kuceyeski A, Kamel H, Navi BB, Raj A, Iadecola C. Predicting Future Brain Tissue Loss From White Matter Connectivity Disruption in Ischemic Stroke. *Stroke*. 2014;45(3):717-722. doi:10.1161/STROKEAHA.113.003645

14. Liang Z, Zeng J, Liu S, et al. A prospective study of secondary degeneration following subcortical infarction using diffusion tensor imaging. *J Neurol Neurosurg Psychiatry*. 2007;78(6):581-586. doi:10.1136/jnnp.2006.099077

15. Zhang J, Zhang Y, Xing S, Liang Z, Zeng J. Secondary Neurodegeneration in Remote Regions After Focal Cerebral Infarction: A New Target for Stroke Management? *Stroke*. 2012;43(6):1700-1705. doi:10.1161/STROKEAHA.111.632448

16. Bowren M, Bruss J, Manzel K, et al. Post-stroke outcomes predicted from multivariate lesion-behaviour and lesion network mapping. *Brain*. 2022;145(4):1338-1353. doi:10.1093/brain/awac010

17. Guggisberg AG, Koch PJ, Hummel FC, Buetefisch CM. Brain networks and their relevance for stroke rehabilitation. *Clin Neurophysiol*. 2019;130(7):1098-1124. doi:10.1016/j.clinph.2019.04.004

18. Liu J, Wang C, Qin W, et al. Cortical structural changes after subcortical stroke: Patterns and correlates. *Hum Brain Mapp*. 2023;44(2):727-743. doi:10.1002/hbm.26095

19. Souter NE, Wang X, Thompson H, et al. Mapping lesion, structural disconnection, and functional disconnection to symptoms in semantic aphasia. *Brain Struct Funct*. 2022;227(9):3043-3061. doi:10.1007/s00429-022-02526-6

20. Veldsman M. Brain Atrophy Estimated from Structural Magnetic Resonance Imaging as a Marker of Large-Scale Network-Based Neurodegeneration in Aging and Stroke. *Geriatrics*. 2017;2(4):34. doi:10.3390/geriatrics2040034

21. Shafiei G, Markello RD, Makowski C, et al. Spatial Patterning of Tissue Volume Loss in Schizophrenia Reflects Brain Network Architecture. *Biol Psychiatry*. 2020;87(8):727-735. doi:10.1016/j.biopsych.2019.09.031

22. Chopra S, Segal A, Oldham S, et al. Network-Based Spreading of Gray Matter Changes Across Different Stages of Psychosis. *JAMA Psychiatry*. 2023;80(12):1246. doi:10.1001/jamapsychiatry.2023.3293

23. Lin Q, Cao D, Li W, et al. Connectome architecture for gray matter atrophy and surgical outcomes in temporal lobe epilepsy. *Epilepsia*. 2025;66(6):2053-2065. doi:10.1111/epi.18343

24. Agosta F, Basaia S, Spinelli EG, et al. Modelling pathological spread through the structural connectome in the frontotemporal dementia clinical spectrum. *Brain*. Published online November 29, 2024:awae391. doi:10.1093/brain/awae391

25. Shafiei G, Bazinet V, Dadar M, et al. Network structure and transcriptomic vulnerability shape atrophy in frontotemporal dementia. *Brain*. 2023;146(1):321-336. doi:10.1093/brain/awac069

26. Shen Y, Wang C, Chen X, et al. Structural Connectome Architecture Shapes Cortical Atrophy in Major Depressive Disorder: A Chinese DIRECT Consortium Study. *Biol Psychiatry*. 2026;99(8):682-691. doi:10.1016/j.biopsych.2025.06.030

27. Grefkes C, Fink GR. Reorganization of cerebral networks after stroke: new insights from neuroimaging with connectivity approaches. *Brain*. 2011;134(5):1264-1276. doi:10.1093/brain/awr033

28. Wu O, Cloonan L, Mocking SJT, et al. Role of Acute Lesion Topography in Initial Ischemic Stroke Severity and Long-Term Functional Outcomes. *Stroke*. 2015;46(9):2438-2444. doi:10.1161/STROKEAHA.115.009643

29. Corbetta M, Ramsey L, Callejas A, et al. Common Behavioral Clusters and Subcortical Anatomy in Stroke. *Neuron*. 2015;85(5):927-941. doi:10.1016/j.neuron.2015.02.027

30. Bayrak Ş, Khalil AA, Villringer K, et al. The impact of ischemic stroke on connectivity gradients. *NeuroImage Clin*. 2019;24:101947. doi:10.1016/j.nicl.2019.101947

31. Joliot M, Jobard G, Naveau M, et al. AICHA: An atlas of intrinsic connectivity of homotopic areas. *J Neurosci Methods*. 2015;254:46-59. doi:10.1016/j.jneumeth.2015.07.013

32. Elam JS, Glasser MF, Harms MP, et al. The Human Connectome Project: A retrospective. *NeuroImage*. 2021;244:118543. doi:10.1016/j.neuroimage.2021.118543

33. Donahue CJ, Sotiropoulos SN, Jbabdi S, et al. Using Diffusion Tractography to Predict Cortical Connection Strength and Distance: A Quantitative Comparison with Tracers in the Monkey. *J Neurosci*. 2016;36(25):6758-6770. doi:10.1523/JNEUROSCI.0493-16.2016

34. Burt JB, Helmer M, Shinn M, Anticevic A, Murray JD. Generative modeling of brain maps with spatial autocorrelation. *NeuroImage*. 2020;220:117038. doi:10.1016/j.neuroimage.2020.117038

35. Alexander-Bloch AF, Shou H, Liu S, et al. On testing for spatial correspondence between maps of human brain structure and function. *NeuroImage*. 2018;178:540-551. doi:10.1016/j.neuroimage.2018.05.070

36. Rubinov M, Kötter R, Hagmann P, Sporns O. Brain connectivity toolbox: a collection of complex network measurements and brain connectivity datasets. *NeuroImage*. 2009;47:S169. doi:10.1016/S1053-8119(09)71822-1

37. Raj A, Kuceyeski A, Weiner M. A Network Diffusion Model of Disease Progression in Dementia. *Neuron*. 2012;73(6):1204-1215. doi:10.1016/j.neuron.2011.12.040

38. Raj A, LoCastro E, Kuceyeski A, Tosun D, Relkin N, Weiner M. Network Diffusion Model of Progression Predicts Longitudinal Patterns of Atrophy and Metabolism in Alzheimer's Disease. *Cell Rep*. 2015;10(3):359-369. doi:10.1016/j.celrep.2014.12.034

39. Liu ZQ, Luppi AI, Hansen JY, et al. Benchmarking methods for mapping functional connectivity in the brain. *Nat Methods*. 2025;22(7):1593-1602. doi:10.1038/s41592-025-02704-4

40. Biswal B, Zerrin Yetkin F, Haughton VM, Hyde JS. Functional connectivity in the motor cortex of resting human brain using echo-planar mri. *Magn Reson Med*. 1995;34(4):537-541. doi:10.1002/mrm.1910340409

41. Deco G, Jirsa VK, McIntosh AR. Emerging concepts for the dynamical organization of resting-state activity in the brain. *Nat Rev Neurosci*. 2011;12(1):43-56. doi:10.1038/nrn2961

42. Honey CJ, Sporns O, Cammoun L, et al. Predicting human resting-state functional connectivity from structural connectivity. *Proc Natl Acad Sci*. 2009;106(6):2035-2040. doi:10.1073/pnas.0811168106

43. Foulon C, Cerliani L, Kinkingnéhun S, et al. Advanced lesion symptom mapping analyses and implementation as BCBtoolkit. *GigaScience*. 2018;7(3). doi:10.1093/gigascience/giy004

44. Griffis JC, Metcalf NV, Corbetta M, Shulman GL. Structural Disconnections Explain Brain Network Dysfunction after Stroke. *Cell Rep*. 2019;28(10):2527-2540.e9. doi:10.1016/j.celrep.2019.07.100

45. Hustings N, Lemmerling M. MRI of Wallerian Degeneration in the Brainstem: A Pictorial Essay. *J Belg Soc Radiol*. 2021;105(1):58. doi:10.5334/jbsr.2585

46. Cao X, Wang Z, Chen X, et al. White matter degeneration in remote brain areas of stroke patients with motor impairment due to basal ganglia lesions. *Hum Brain Mapp*. 2021;42(14):4750-4761. doi:10.1002/hbm.25583

47. Conforti L, Gilley J, Coleman MP. Wallerian degeneration: an emerging axon death pathway linking injury and disease. *Nat Rev Neurosci*. 2014;15(6):394-409. doi:10.1038/nrn3680

48. Lima RR, Oliveira ACA, Fernandes RM, Nascimento PC, Freire MAM, Gomes-Leal W. Inflammatory Response and Secondary White Matter Damage to the Corpus Callosum after Focal Striatal Stroke in Rats. *Int J Mol Sci*. 2022;23(6):3179. doi:10.3390/ijms23063179

49. Coleman MP, Höke A. Programmed axon degeneration: from mouse to mechanism to medicine. *Nat Rev Neurosci*. 2020;21(4):183-196. doi:10.1038/s41583-020-0269-3

50. Duering M, Righart R, Wollenweber FA, Zietemann V, Gesierich B, Dichgans M. Acute infarcts cause focal thinning in remote cortex via degeneration of connecting fiber tracts. *Neurology*. 2015;84(16):1685-1692. doi:10.1212/WNL.0000000000001502

51. Cowan WM. Anterograde and Retrograde Transneuronal Degeneration in the Central and Peripheral Nervous System. In: Nauta WJH, Ebbesson SOE, eds. *Contemporary Research Methods in Neuroanatomy*. Springer Berlin Heidelberg; 1970:217-251. doi:10.1007/978-3-642-85986-1_11

52. Waller A. Experiments on the Section of the Glosso-Pharyngeal and Hypoglossal Nerves of the Frog, and Observations of the Alterations Produced Thereby in the Structure of Their Primitive Fibres. *Edinb Med Surg J*. 1851;76(189):369-376.

53. Crespi F, Guidali G, Melzi L, Bianchi Marzoli S, Bolognini N. Trans-Synaptic Retrograde Retinal Degeneration After Post-Chiasmatic Stroke: A Systematic Review of Empirical Evidence. *Eur J Neurol*. 2026;33(4):e70566. doi:10.1111/ene.70566

54. Canudas AM, Pezzi S, Canals JM, Pallàs M, Alberch J. Endogenous brain-derived neurotrophic factor protects dopaminergic nigral neurons against transneuronal degeneration

induced by striatal excitotoxic injury. *Mol Brain Res*. 2005;134(1):147-154. doi:10.1016/j.molbrainres.2004.11.012

55. Carrera E, Tononi G. Diaschisis: past, present, future. *Brain J Neurol*. 2014;137(Pt 9):2408-2422. doi:10.1093/brain/awu101

56. Cheng B, Schulz R, Bönstrup M, et al. Structural plasticity of remote cortical brain regions is determined by connectivity to the primary lesion in subcortical stroke. *J Cereb Blood Flow Metab*. 2015;35(9):1507-1514. doi:10.1038/jcbfm.2015.74

57. Kancheva I, Buma F, Kwakkel G, Kancheva A, Ramsey N, Raemaekers M. Investigating secondary white matter degeneration following ischemic stroke by modelling affected fiber tracts. *NeuroImage Clin*. 2022;33:102945. doi:10.1016/j.nicl.2022.102945

58. Cheng B, Dietzmann P, Schulz R, et al. Cortical atrophy and transcallosal diaschisis following isolated subcortical stroke. *J Cereb Blood Flow Metab*. 2020;40(3):611-621. doi:10.1177/0271678X19831583

59. Brodtmann A, Khlif MS, Egorova N, Veldsman M, Bird LJ, Werden E. Dynamic Regional Brain Atrophy Rates in the First Year After Ischemic Stroke. *Stroke*. 2020;51(9). doi:10.1161/STROKEAHA.120.030256

60. Thomalla G, Glauche V, Weiller C, Röther J. Time course of wallerian degeneration after ischaemic stroke revealed by diffusion tensor imaging. *J Neurol Neurosurg Psychiatry*. 2005;76(2):266-268. doi:10.1136/jnnp.2004.046375

61. Carmichael ST. The 3 Rs of Stroke Biology: Radial, Relayed, and Regenerative. *Neurotherapeutics*. 2016;13(2):348-359. doi:10.1007/s13311-015-0408-0

62. Anrather J, Iadecola C. Inflammation and Stroke: An Overview. *Neurotherapeutics*. 2016;13(4):661-670. doi:10.1007/s13311-016-0483-x

63. Gu Y, Zhou C, Piao Z, et al. Cerebral edema after ischemic stroke: Pathophysiology and underlying mechanisms. *Front Neurosci*. 2022;16:988283. doi:10.3389/fnins.2022.988283

64. Cramer SC. Repairing the human brain after stroke: I. Mechanisms of spontaneous recovery. *Ann Neurol*. 2008;63(3):272-287. doi:10.1002/ana.21393

65. Wang JT, Toh B, An J, et al. Loss of Sarm1 Mitigates Axonal Degeneration and Promotes Neuronal Repair After Ischemic Stroke. *bioRxiv*. Published online February 25, 2025:2025.02.20.639171. doi:10.1101/2025.02.20.639171

66. Aerts H, Fias W, Caeyenberghs K, Marinazzo D. Brain networks under attack: robustness properties and the impact of lesions. *Brain*. 2016;139(12):3063-3083. doi:10.1093/brain/aww194

67. Crossley NA, Mechelli A, Scott J, et al. The hubs of the human connectome are generally implicated in the anatomy of brain disorders. *Brain*. 2014;137(8):2382-2395. doi:10.1093/brain/awu132

68. Aguiar RPD, Newman-Tancredi A, Prickaerts J, Oliveira RMWD. The 5-HT1A receptor as a serotonergic target for neuroprotection in cerebral ischemia. *Prog Neuropsychopharmacol Biol Psychiatry*. 2021;109:110210. doi:10.1016/j.pnpbp.2020.110210

69. Aguiar RP, Soares LM, Meyer E, et al. Activation of 5-HT1A postsynaptic receptors by NLX-101 results in functional recovery and an increase in neuroplasticity in mice with brain ischemia. *Prog Neuropsychopharmacol Biol Psychiatry*. 2020;99:109832. doi:10.1016/j.pnpbp.2019.109832

70. Olesen OF, Bennike B, Dam H, Mellerup E. Association of the 5-HT2A Receptor Gene Polymorphism 102T/C With Ischemic Stroke. *J Mol Neurosci*. 2006;30(3):323-328. doi:10.1385/JMN:30:3:323

71. Koch PJ, Frey BM, Backhaus W, et al. Neurotransmitter-informed connectivity maps and their application for outcome inference after stroke. *Brain*. 2025;148(11):3935-3945. doi:10.1093/brain/awaf185

72. Koch PJ, Park CH, Girard G, et al. The structural connectome and motor recovery after stroke: predicting natural recovery. *Brain*. 2021;144(7):2107-2119. doi:10.1093/brain/awab082

73. Dawson J, Liu CY, Francisco GE, et al. Vagus nerve stimulation paired with rehabilitation for upper limb motor function after ischaemic stroke (VNS-REHAB): a randomised, blinded, pivotal, device trial. *The Lancet*. 2021;397(10284):1545-1553. doi:10.1016/S0140-6736(21)00475-X

74. Bonkhoff AK, Grefkes C. Precision medicine in stroke: towards personalized outcome predictions using artificial intelligence. *Brain*. 2022;145(2):457-475. doi:10.1093/brain/awab439

75. Kumar S, Ferraro M, Nguyen L, et al. TMS assessment of corticospinal tract integrity after stroke: broadening the concept to inform neurorehabilitation prescription. *Front Hum Neurosci*. 2024;18:1408818. doi:10.3389/fnhum.2024.1408818

76. Siegel JS, Seitzman BA, Ramsey LE, et al. Re-emergence of modular brain networks in stroke recovery. *Cortex*. 2018;101:44-59. doi:10.1016/j.cortex.2017.12.019

77. Salvalaggio A, De Filippo De Grazia M, Zorzi M, Thiebaut de Schotten M, Corbetta M. Post-stroke deficit prediction from lesion and indirect structural and functional disconnection. *Brain*. 2020;143(7):2173-2188. doi:10.1093/brain/awaa156

78. Chen Y, Jiang Y, Kong X, et al. Common and unique structural plasticity after left and right hemisphere stroke. *J Cereb Blood Flow Metab*. 2021;41(12):3350-3364. doi:10.1177/0271678X211036606

79. Robb RA. A Software System for Interactive and Quantitative Analysis of Biomedical Images. In: Höhne KH, Fuchs H, Pizer SM, eds. *3D Imaging in Medicine*. Springer; 1990:333-361. doi:10.1007/978-3-642-84211-5_22

80. Rowland DJ, Garbow JR, Laforest R, Snyder AZ. Registration of [18F]FDG microPET and small-animal MRI. *Nucl Med Biol*. 2005;32(6):567-572. doi:10.1016/j.nucmedbio.2005.05.002

81. Jenkinson M, Beckmann CF, Behrens TEJ, Woolrich MW, Smith SM. FSL. *NeuroImage*. 2012;62(2):782-790. doi:10.1016/j.neuroimage.2011.09.015

82. Ashburner J. Symmetric diffeomorphic modeling of longitudinal structural MRI. *Front Neurosci*. 2013;6. doi:10.3389/fnins.2012.00197

83. Crinion J, Ashburner J, Leff A, Brett M, Price C, Friston K. Spatial normalization of lesioned brains: Performance evaluation and impact on fMRI analyses. *NeuroImage*. 2007;37(3):866-875. doi:10.1016/j.neuroimage.2007.04.065

84. Douaud G, Groves AR, Tamnes CK, et al. A common brain network links development, aging, and vulnerability to disease. *Proc Natl Acad Sci*. 2014;111(49):17648-17653. doi:10.1073/pnas.1410378111

85. Bethlehem RAI, Seidlitz J, White SR, et al. Brain charts for the human lifespan. *Nature*. 2022;604(7906):525-533. doi:10.1038/s41586-022-04554-y

86. Fan L, Li H, Zhuo J, et al. The Human Brainnetome Atlas: A New Brain Atlas Based on Connectional Architecture. *Cereb Cortex*. 2016;26(8):3508-3526. doi:10.1093/cercor/bhw157

87. Glasser MF, Sotiropoulos SN, Wilson JA, et al. The minimal preprocessing pipelines for the Human Connectome Project. *NeuroImage*. 2013;80:105-124. doi:10.1016/j.neuroimage.2013.04.127

88. Zhao C, Yang L, Xie S, Zhang Z, Pan H, Gong G. Hemispheric Module-Specific Influence of the X Chromosome on White Matter Connectivity: Evidence from Girls with Turner Syndrome. *Cereb Cortex*. 2019;29(11):4580-4594. doi:10.1093/cercor/bhy335

89. Shafiei G, Markello RD, Makowski C, et al. Spatial Patterning of Tissue Volume Loss in Schizophrenia Reflects Brain Network Architecture. *Biol Psychiatry*. 2020;87(8):727-735. doi:10.1016/j.biopsych.2019.09.031

90. Vo A, Tremblay C, Rahayel S, et al. Global network and local vulnerabilities underlie brain atrophy across Parkinson's disease stages. *Brain*. Published online November 14, 2025:awaf432. doi:10.1093/brain/awaf432

91. Váša F, Mišić B. Null models in network neuroscience. *Nat Rev Neurosci*. 2022;23(8):493-504. doi:10.1038/s41583-022-00601-9

92. Kruskal WH, Wallis WA. Use of Ranks in One-Criterion Variance Analysis. *J Am Stat Assoc*. 1952;47(260):583-621. doi:10.1080/01621459.1952.10483441

93. Mann HB, Whitney DR. On a Test of Whether one of Two Random Variables is Stochastically Larger than the Other. *Ann Math Stat*. 1947;18(1):50-60.

94. Dunn OJ. Multiple Comparisons among Means. *J Am Stat Assoc*. 1961;56(293):52-64. doi:10.1080/01621459.1961.10482090

95. Hansen JY, Shafiei G, Markello RD, et al. Mapping neurotransmitter systems to the structural and functional organization of the human neocortex. *Nat Neurosci*. 2022;25(11):1569-1581. doi:10.1038/s41593-022-01186-3

96. Markello RD, Hansen JY, Liu ZQ, et al. neuromaps: structural and functional interpretation of brain maps. *Nat Methods*. 2022;19(11):1472-1479. doi:10.1038/s41592-022-01625-w

97. Winkler AM, Ridgway GR, Webster MA, Smith SM, Nichols TE. Permutation inference for the general linear model. *NeuroImage*. 2014;92:381-397. doi:10.1016/j.neuroimage.2014.01.060

98. Genovese CR, Lazar NA, Nichols T. Thresholding of Statistical Maps in Functional Neuroimaging Using the False Discovery Rate. *NeuroImage*. 2002;15(4):870-878. doi:10.1006/nimg.2001.1037

99. Hoerl AE, Kennard RW. Ridge Regression: Biased Estimation for Nonorthogonal Problems. *Technometrics*. 1970;12(1):55-67. doi:10.1080/00401706.1970.10488634

100. Cui Z, Gong G. The effect of machine learning regression algorithms and sample size on individualized behavioral prediction with functional connectivity features. *NeuroImage*. 2018;178:622-637. doi:10.1016/j.neuroimage.2018.06.001

101. Valente G, Castellanos AL, Hausfeld L, De Martino F, Formisano E. Cross-validation and permutations in MVPA: Validity of permutation strategies and power of cross-validation schemes. *NeuroImage*. 2021;238:118145. doi:10.1016/j.neuroimage.2021.118145

Supplementary Files

This is a list of supplementary files associated with this preprint. Click to download.

- Supplementary.pdf